machines

MDPI

Article

Enhancing Self-Starting Capability and Efficiency of Hybrid Darrieus–Savonius Vertical Axis Wind Turbines with a Dual-Shaft Configuration

Farzad Ghafoorian, Sina Hosseini Rad and Mahdi Moghimi *

School of Mechanical Engineering, Iran University of Science and Technology, Tehran 16846-13114, Iran; farzadghafoorianiust@gmail.com (F.G.); sinahosseinirad28@gmail.com (S.H.R.)
* Correspondence: moghimi@iust.ac.ir

Abstract: Self-starting capability has consistently presented a significant challenge for Darrieus vertical axis wind turbines (VAWTs). One advantageous approach to addressing this problem is the design of a hybrid Darrieus–Savonius VAWT. The hybrid VAWT enhances self-starting capability by increasing the power coefficient (C_p) within the low tip speed ratio (TSR) range and the torque coefficient (C_m) at initial azimuth angles, when the blades transition from windward to upwind position. A significant challenge associated with conventional hybrid VAWTs, in which both rotors are mounted on a single shaft, is the decline in efficiency at the high-TSR range. This inefficiency is due to the performance limitations of the inner Savonius rotor, which is designed to function at low angular velocities. In the high-TSR range, the vorticity generation around Savonius rotor buckets adversely impacts the Darrieus rotor performance and the hybrid VAWT. A dual-shaft configuration is proposed to mitigate this issue, which utilizes a drivetrain transmission system to prevent the Savonius rotor from exceeding its optimal angular velocity, thus acting as a control mechanism. The findings indicate that implementing the dual-shaft rotor resulted in a 35% improvement in C_p within the low-TSR range and a 25% enhancement in the high-TSR range. This improvement is achieved when the inner rotor's angular velocity is maintained at 19.79 rad/s, which has been determined to be the optimal value for the inner rotor.

Keywords: hybrid Darrieus–Savonius VAWT; single-shaft rotor; dual-shaft rotor; low- and high-TSR range

check for updates

Academic Editor: Davide Astolfi

Received: 30 December 2024
Revised: 17 January 2025
Accepted: 22 January 2025
Published: 23 January 2025

Citation: Ghafoorian, F.; Hosseini Rad, S.; Moghimi, M. Enhancing Self-Starting Capability and Efficiency of Hybrid Darrieus–Savonius Vertical Axis Wind Turbines with a Dual-Shaft Configuration. *Machines* **2025**, *13*, 87. https://doi.org/10.3390/machines13020087

Copyright: © 2025 by the authors. Licensee MDPI, Basel, Switzerland. This article is an open access article distributed under the terms and conditions of the Creative Commons Attribution (CC BY) license (https://creativecommons.org/licenses/by/4.0/).

1. Introduction

The unacceptable rise in greenhouse gas emissions from fossil fuels has propelled the development of renewable energy sources. Wind energy is considered a clean and sustainable option for meeting energy needs [1]. The rapid advancement of wind energy has led to an increased adoption of wind turbines, along with technological improvements and innovative designs [2]. Vertical-axis wind turbines (VAWTs) are becoming a practical alternative to traditional horizontal-axis wind turbines (HAWTs) due to their smaller size and lower installation and maintenance costs. VAWTs offer advantages such as independence from wind direction, which improves efficiency in different conditions [3]. According to the aerodynamic forces, VAWTs are classified into two primary categories: lift-based designs, such as the Darrieus and Gorlov VAWTs, and drag-based designs, exemplified by the Savonius VAWT [4]. Savonius VAWTs operate like impulse turbines, using pressure differentials across their buckets. They have low efficiency and limited operational range but do not

require initial torque for self-starting [5]. Darrieus VAWTs use the pressure differential between the suction and pressure sides of the blade to provide a wider operating range and higher efficiency than drag-based turbines. However, they require an initial torque to start and cannot self-start, limiting their functional application [6]. Savonius turbines are most efficient at the low-TSR range and function competently at low angular velocities. In contrast, Darrieus VAWTs perform best in the high-TSR range. Therefore, Savonius VAWTs have better self-starting capability than Darrieus VAWTs due to their performance in the low-TSR range [7].

Solutions for enhancing self-starting capability in Darrieus VAWTs focus on rotor optimization, including auxiliary blades and hybrid or dual rotor designs [8]. Dual-rotor Darrieus VAWTs can be configured where one rotor is either mounted above the other or the inner rotor is covered by another. These arrangements are commonly referred to as co-axial configurations [9]. The co-axial configuration of two Darrieus rotors, which covered each other, was examined, revealing an improvement in the torque coefficient of 300%. This enhancement subsequently conferred the improvement in self-starting capability [10]. Another study on co-axial two-stage Darrieus VAWTs indicated that this design could enhance the power coefficient up to 130% within the low-TSR range in comparison to the conventional configuration [11]. Another optimization of the rotor involves the integration of a lift-based Darrieus VAWT with a drag-based Savonius VAWT drag. This coupling aims to enhance the self-starting capability by increasing the rotor torque within the low-TSR range [12]. The hybrid Darrieus–Savonius configuration can be engineered with one rotor situated above the other, allowing for two- or multi-stage arrangements, or alternatively, with the Darrieus rotor covering the Savonius rotor [13]. Hosseini et al. [14] demonstrated that a hybrid Darrieus–Savonius VAWT achieved improvements of 120% in C_p and 80% in C_m at a TSR of 1 when compared to solo conventional Darrieus VAWT. This enhancement in efficiency within the low-TSR range signifies a notable advancement in the self-starting capability of the hybrid configuration. In the same CFD investigation, Roshan et al. [15] reported a remarkable 400% enhancement in C_p at the initial TSR of 0.5, further illustrating the self-starting capability improvement of the hybrid rotor. A CFD study conducted by Asadi and Hassanzadeh [16] demonstrated that the total average C_p of the hybrid rotor is 10% greater than that of the single Darrieus rotor. However, the hybrid configuration exhibited the most significant C_m enhancement at the initial TSR = 1.5. This finding underscores the hybrid configuration's effectiveness in improving self-starting capabilities. The primary reason for the reduced efficiency of the hybrid configuration at high angular velocities is attributed to the adverse impact of the vorticities generated around the Savonius VAWT buckets on the Darrieus rotor blades. This phenomenon becomes more pronounced at the high-TSR range, where the effects of vorticity magnitude are more evident [17]. In addressing this issue, Abdelsalam et al. [18] evaluated the attachment angle and the diameter ratio of the Darrieus and Savonius rotors to mitigate the adverse interactions between the two rotors. The findings indicate that a diameter ratio of 0.43 and an attachment angle of 30° represent the most optimal design parameters for hybrid VAWTs. Kumar et al. [19] demonstrated that a hybrid configuration employing a large-diameter Savonius rotor exhibits superior performance compared to a hybrid rotor utilizing a small Savonius rotor within the low-TSR range. However, in the high-TSR range, the enlarged diameter of the inner rotor induces vorticity in the vicinity of the Darrieus rotor, resulting in a significant reduction in C_p up to 114% at TSR = 4. In addition to the attachment angle and the diameter ratio, Zhang et al. [20] demonstrated through a CFD and sensitivity analysis that the pitch angle of the Darrieus rotor is not only a significant design parameter but also exerts a greater influence than the other two parameters, about 27%. To mitigate the impact of the vorticity magnitude surrounding the Savonius buckets on the

Darrieus rotor, a design incorporating two rotors configured in a dual-stage arrangement can be implemented, instead of the Darrieus rotor covering the inner rotor [21]. The findings indicate that positioning the Savonius rotor above the helical Darrieus rotor resulted in a 128% enhancement in C_p within the higher TSR range [22].

In dual-rotor configurations of Darrieus and Savonius VAWTs or hybrid Darrieus–Savonius designs, the direction of rotor rotation is a critical factor. This is particularly significant in both single- and multi-stage co-axial arrangements of Darrieus and Savonius turbines [23]. Research findings regarding multi-stage Savonius counter-rotating (CR) VAWTs indicate that in a two-stage configuration, the operation of the rotors in a counter-rotating manner results in a notable increase in both the torque and power output of the turbine assembly when compared to a single Savonius VAWT [24]. Didane et al. [25] evaluated a hybrid Darrieus–Savonius CR-VAWT configuration. Their findings indicate that the performance of the counter-rotating VAWT configuration demonstrated significant improvement in power and self-starting capability compared to that of the individual Darrieus and Savonius rotors. In conjunction with their prior experimental findings, the CFD results presented by Didane et al. [26] have substantiated the performance enhancement of the hybrid Darrieus–Savonius CR-VAWT configuration. This configuration demonstrated a C_p increase of 75% and 133%, respectively, compared to the upper and lower rotors. It is essential to highlight that the configuration of the two-stage Darrieus CR-VAWT exhibits a significant distinction from hybrid Darrieus–Savonius configurations or co-axial dual Darrieus configurations, where one rotor is covered by another. Specifically, the two-stage Darrieus CR-VAWT experiences a 90% reduction in the C_p at elevated rotational velocities compared to the two-stage Darrieus VAWT operating at an identical rotation direction [27]. The design specifications of CR-VAWTs play a crucial role in determining the specialized configuration of their drivetrains. In co-axial configurations, separating the energy generation (EG) components is unnecessary. In co-axial CR-VAWTs, the drivetrain designs may be identical, as the mechanical differences among these categories primarily pertain to the relative positioning of their rotors [28]. The findings suggest that rigid transmission with gears provides advantages in initiating and maintaining stable operation, though it suffers from backlash, leading to oscillations due to spring-like torques. In contrast, gearless transmission is simple and reliable, effectively reducing mechanical vibrations in long and flexible rotor shafts. However, it is sensitive to variations in rotor inertia and wind speed fluctuations. The rigid transmission offers greater stability under these conditions compared to gearless systems. Consequently, while gearless transmission is a promising option for CR-VAWTs, there remains a need to develop new strategies for stabilizing Wind Energy Conversion Systems (WECSs) [29,30]. Conventional rigid gearbox systems are suitable transmission systems for co-axial VAWTs with constant angular velocities for inner and outer rotors, focusing on mechanical stability. These systems feature a double epicyclic cluster gear arrangement, utilizing type B for the gear hub [31].

As outlined in the literature review, the self-starting capability presents a significant challenge for Darrieus VAWTs. A promising approach to address this issue is the utilization of hybrid Darrieus–Savonius VAWTs. However, a primary concern remains the reduction in efficiency and the disturbance to the aerodynamic performance of hybrid rotors within the high-TSR range. This issue constitutes a fundamental research gap not addressed in previous studies. This study thoroughly investigates the factors contributing to the decline in efficiency of conventional hybrid rotors characterized by a single-shaft design, wherein both rotors are mounted on the same shaft. After analyzing the inefficiencies associated with single-shaft hybrid configurations, the study explores dual-shaft hybrid configurations as a potential solution. The proposed approach involves the utilization of a drivetrain transmission system to regulate the angular velocity of the inner Savonius

rotor. This regulation is achieved through a reliable control system that prevents the inner rotor from exceeding its angular velocity limit, precisely calibrated for low revolutions. In the forthcoming phase of this research, a comparative analysis of co-rotating and counter-rotating configurations for the dual-shaft rotor will be undertaken. This study presents the dual-shaft hybrid Darrieus–Savonius VAWT and introduces a transmission mechanism that serves as a control system to ensure that the angular velocity of the inner Savonius rotor is maintained within a defined range for the first time. Additionally, the assessment of both operational manners, co-rotation and counter-rotation, offers a novel contribution to the existing body of knowledge. The primary motivation behind developing a dual-shaft hybrid configuration of Darrieus–Savonius VAWTs is the efficiency challenges of conventional single-shaft designs, particularly in the high-TSR range. This study proposes a control mechanism to regulate the angular velocity of the Savonius rotor, which is inherently designed to function optimally at low angular velocities. By implementing this solution, the study addresses the efficiency limitations of hybrid rotors at elevated angular velocities. The authors of this research are introducing this innovative approach for the first time.

2. Case Study Discretion

This investigation aims to evaluate a model of a hybrid Darrieus–Savonius VAWT, operating under the premise that the Savonius and Darrieus rotors are independent concerning their rotational axes. The hybrid rotor is categorized as a co-axial VAWT. The distinction between the single-shaft hybrid configuration and the dual-shaft hybrid configuration lies in the independence of their axes of rotation. Although both configurations are co-axial, dual-shaft configurations are not mounted on a shared shaft like single-shaft configurations. By incorporating a drivetrain transmission system, dual-shaft configurations can operate at varying angular velocities, thereby ensuring that the angular velocity of the Savonius rotor remains above a specified threshold. This configuration is designed to regulate Savonius rotor angular velocity to prevent any adverse effects from the vortices generated around the buckets of the Savonius rotor at high-TSR impacting the performance of the Darrieus rotor. Also, for the hybrid Darrieus–Savonius CR-VAWT, the positioning of the Savonius rotor is mirrored on its center of rotation. Moreover, a transmission system and gear mechanism are still utilized to regulate the angular velocity of the Savonius rotor in hybrid CR-VAWT.

2.1. Hybrid VAWT Design

In this simulation, the CAD models developed for the Darrieus VAWT by Castelli et al. [32] and the Savonius VAWT model created by Wenehenubun et al. [33] were utilized to design the hybrid rotor. This design is shown in Figure 1, alongside the simulation process from model selection and CAD development to post-processing, and its specifications are detailed in Table 1.

Table 1. Hybrid Darrieus–Savonius VAWT Dimensions.

Parameter	Darrieus VAWT	Savonius VAWT
Number of blades	3	2
Rotor diameter	1030 (mm)	370 (mm)
Blade chord length	85.8 (mm)	-
Darrieus rotor solidity	0.5	-
Overlap size	-	30 (mm)
Bucker diameter	-	200 (mm)
Bucket thickness	-	2 (mm)

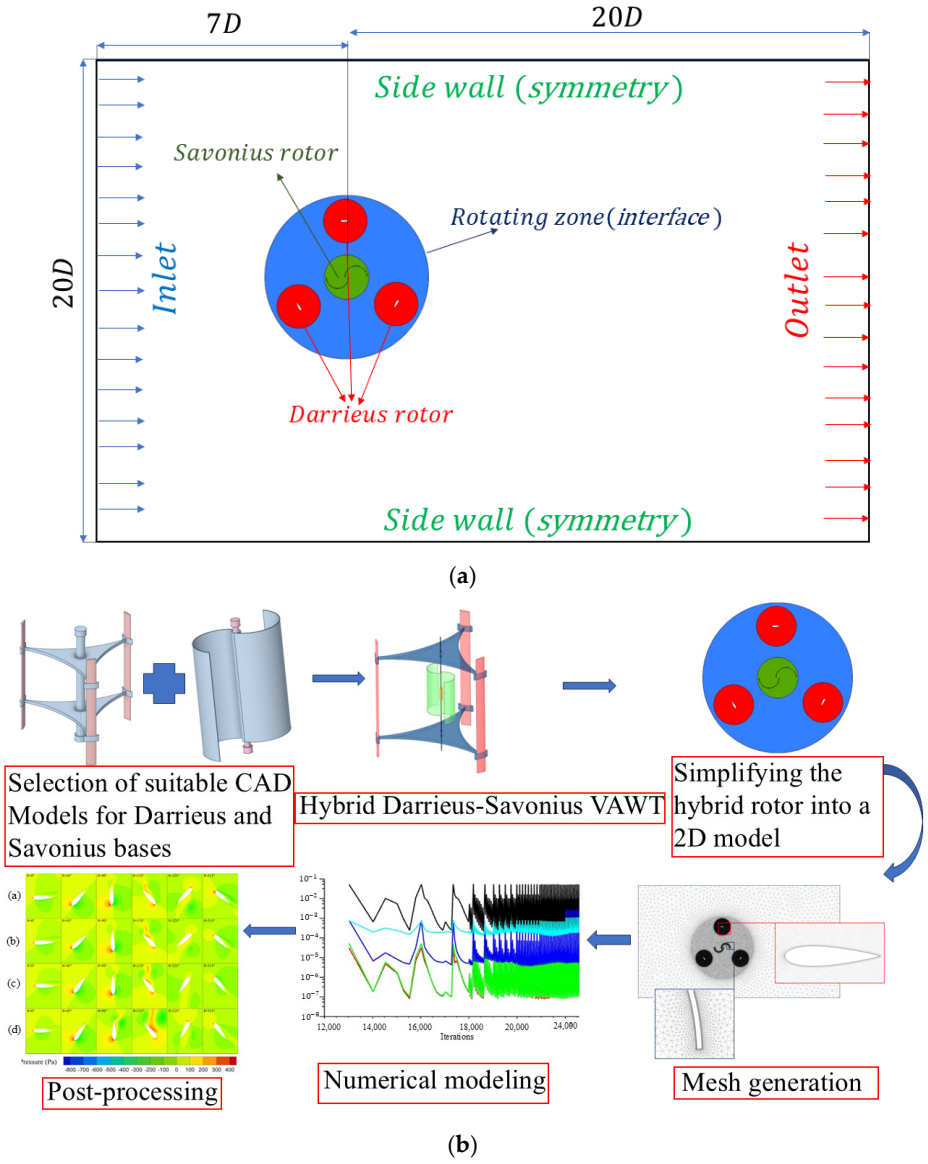
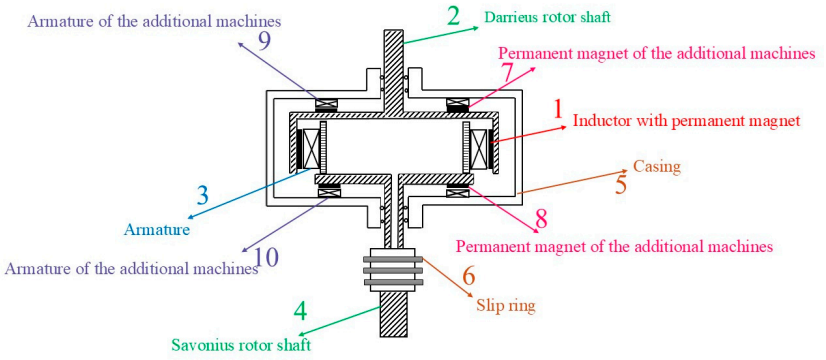


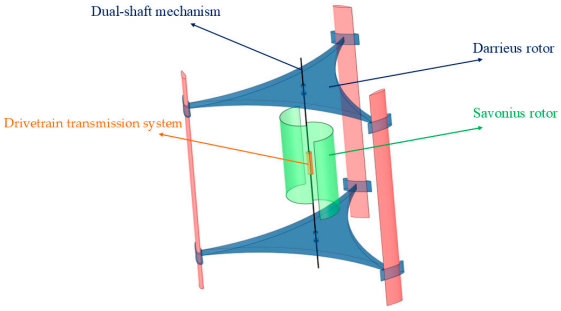
Figure 1. (**a**) Computational domain and boundary conditions. (**b**) Simulation process.

2.2. Drivetrain Transmission System

While gearless drivetrain transmission systems exhibit instability under varying wind speeds, angular velocities, and sensitivity to the rotor's moments of inertia and wind gusts, they offer enhanced reliability compared to conventional rigid transmissions. This reliability is attributed to the absence of backlash and spring-like adverse effects between system gears, which can occur in the rigid transmissions of co-axial VAWTs with elongated rotor shafts. Another advantage of the gearless transmission is its capability to provide a control mechanism for hybrid VAWT, which requires the inner rotor with a reduced angular velocity [9]. Considering the various advantages of gearless drivetrain transmission systems, which exhibit significantly fewer mechanical repercussions than traditional gearbox systems, this study more confidently does not consider the adverse effects and losses associated with the control system in CFD simulation. As a result, a gearless transmission was chosen for this hybrid CR-VAWT to act as the control system for the Savonius rotor, preventing its angular velocity from exceeding a specific value. A schematic diagram of the drivetrain transmission system is presented in Figure 2. In addition, a diagram of a hybrid rotor, along with a proposed location for the drivetrain transmission system installation, is provided.



(**a**)



(**b**)

Figure 2. (**a**) Sketch of transmission system. (**b**) Hybrid configuration with drivetrain transmission system.

According to Figure 2b, the drivetrain transmission system is positioned centrally along the rotating axis of the hybrid co-axial rotor, allowing the inner and outer rotor shafts to be independently and freely accommodated. The gearless transmission mechanism features an inductor with permanent magnets (1) connected to the primary rotor's shaft, (2) which is a Darrieus rotor, while the armature (3) links to secondary rotor's shaft, which is a Savonius rotor (4). Both shafts can rotate independently within their casing (5). Slip rings (6) supply power to the armature winding (3). Additionally, two low-power synchronous electric machines with permanent magnets (7 and 8) on the rotors and armatures (9 and 10) in the casing enable electromagnetic coupling between the moving rotors and their casing (5). By managing additional electric generator/motor machines, small torques can be generated between the axes of two rotors and their common casing, introducing two load control channels. The stabilization of the hybrid CR-VAWT is achieved by adjusting the torque between the Darrieus and Savonius rotors, allowing one rotor to assist the other while reducing its own torque. This enables one machine to function as a motor and the other as a generator, allowing them to draw power from each other and requiring external power only to offset energy losses, enhancing overall efficiency. These motors/generators also aid in the initial acceleration of the rotors during startup. Adopting a gearless transmission system featuring components designed to facilitate the separation of rotor shafts has enabled the dual-shaft rotor configuration to operate with independent angular velocities for each rotor. In this context, the inner and outer rotors are represented by the Savonius and Darrieus rotors, respectively. This configuration contrasts with the single-shaft system, where both rotors are restricted to a uniform angular velocity. The gearless transmission system permits the independent adjustment of the angular velocity of each rotor. Consequently, it becomes feasible to regulate the rotational velocity of the inner Savonius rotor to a lower threshold than that of the outer Darrieus rotor. This is attributable

to the design of Savonius rotors, which are designed for operation at low angular velocities; their efficiency diminishes at higher angular velocities. In contrast, Darrieus rotors require an initial torque to start operating at low angular velocities. This configuration ultimately maximizes the advantages inherent in the gearless transmission design, serving as a control mechanism to enhance the performance of hybrid VAWTs. Furthermore, this gearless transition system has no drawbacks associated with conventional gearbox mechanisms.

3. Governing Equations and Numerical Setup

3.1. Fluid Mechanics Equations

The Unsteady Reynolds-Averaged Navier–Stokes (URANS) equation is an essential analytical tool for fluid dynamics analysis. It effectively models turbulent flow as an enhanced version of the Reynolds-Averaged Navier–Stokes (RANS) equations, incorporating unsteady terms. The Navier–Stokes equations elucidate the relationships between velocity and pressure in a flow field using a time-averaging approach to quantify turbulence, grounded in Newton's laws of motion and the principles of momentum conservation and continuity. The URANS equation is as follows [34]:

$$\frac{\partial \overline{u_i}}{\partial x_i} = 0 \tag{1}$$

$$\frac{\partial \overline{u_i}}{\partial t} + \frac{\partial}{\partial x_j}\left(\overline{u_i u_j}\right) = -\frac{1}{\rho}\frac{\partial \overline{p}}{\partial x_i} + \frac{\partial}{\partial x_i}\left(\nu \frac{\partial \overline{u_i}}{\partial t} - \overline{u_i' u_j'}\right) \tag{2}$$

Equation (1) denotes the continuity equation responsible for mass conservation within a fluid domain, while Equation (2) outlines the momentum equation, encompassing the fundamental principles of force, mass, and acceleration. $\overline{u_i}$ $(\mathrm{m/s})$ and $\overline{u_j}$ $(\mathrm{m/s})$ represent initial velocity components in a Cartesian coordinate system. Also, ${u'}_i$ $(\mathrm{m/s})$ and ${u'}_j$ $(\mathrm{m/s})$ are fluctuating velocities, vital for assessing turbulence and uncertainties. Additionally, the average pressure $\overline{p}$ $\left(\mathrm{N/m^2}\right)$, density ρ $\left(\mathrm{kg/m^3}\right)$, and kinematic viscosity ν $\left(\mathrm{m^2/s}\right)$ characterize the fluid's properties. The term $\overline{{u'}_i {u'}_j}$, representing Reynolds stress, illustrates the correlation between fluctuating variables in separate velocity components, offering insights into momentum transformations caused by turbulence.

3.2. Turbulence Modeling Equations

The performance of rotor blades in fluid flow is notably influenced by Reynolds stress, making the selection of a suitable turbulence model essential for reliable simulations. Standard approaches, such as $k-\varepsilon$ and $k-\omega$, utilize transport equations for turbulent flow analysis. $k-\varepsilon$ model faces challenges in predicting pressure gradients in turbomachinery due to empirical damping functions. Conversely, the $k-\omega$ model is more effective near wall surfaces but is limited by turbulence conditions. The shear stress transport (SST) $k-\omega$ hybrid model improves predictive accuracy by combining the advantages of the $k-\varepsilon$ model for distant flows with those of the $k-\omega$ model for flows near walls. Here, k $(\frac{\mathrm{m^2}}{\mathrm{s^2}})$ denotes turbulent kinetic energy, and ω $(\mathrm{s^{-1}})$ represents the energy dissipation rate due to viscosity. (SST) $k-\omega$ equations are defined as follows [32]:

$$\rho\frac{d}{dt}(k) + \rho\nabla\cdot\left[k\left(\vec{u} - \vec{u}_g\right)\right] = \nabla\cdot\left[\left(\mu + \frac{\mu_t}{\sigma_k}\right)\nabla k\right] + G_k - Y_k \tag{3}$$

$$\rho\frac{d}{dt}(\omega) + \rho\nabla\cdot\left[\omega\left(\vec{u} - \vec{u}_g\right)\right] = \nabla\cdot\left[\left(\mu + \frac{\mu_t}{\sigma_\omega}\right)\nabla \omega\right] + G_\omega - Y_\omega \tag{4}$$

where Y_k $\left(\frac{\text{kg}}{\text{m}^3 \cdot \text{s}^3}\right)$ and G_k $\left(\frac{\text{kg}}{\text{m}^3 \cdot \text{s}^3}\right)$ are the dissipation and turbulence kinetic energy production, respectively, and G_ω $\left(\frac{1}{\text{m}^3 \cdot \text{s}^3}\right)$ and Y_ω $\left(\frac{1}{\text{m}^3 \cdot \text{s}^3}\right)$ denote ω specific generation and dissipation, respectively. The Prandtl numbers for k and ω are indicated as σ_k and σ_ω, respectively.

3.3. Turbine Mathematical Relations

The effectiveness of VAWTs can be assessed by mathematically estimating the C_p and C_m coefficients from the power generated by the rotor [35].

$$C_p = \frac{P}{\frac{1}{2}\rho \cdot A \cdot V_\infty^3.} \tag{5}$$

$$C_m = \frac{P}{\frac{1}{4}\rho \cdot D^2 \cdot H \cdot V_\infty^2} \tag{6}$$

The total power is represented by P $\left(\frac{\text{N}\cdot\text{m}}{\text{s}}\right)$, where ρ $\left(\frac{\text{kg}}{\text{m}^3}\right)$ is the air density specifically at a standard value of 1.225 $\left(\frac{\text{kg}}{\text{m}^3}\right)$. V_∞ $\left(\frac{\text{m}}{\text{s}}\right)$ denotes the wind velocity coming to the rotor, and the rotor swept area A (m^2) is determined by multiplying the height and diameter of the turbine.

Turbine tip speed ratio is calculated as follows [35]:

$$TSR = \frac{R \cdot \Omega}{V_\infty} \tag{7}$$

where Ω $\left(\frac{\text{rad}}{\text{s}}\right)$ is the turbine rotational velocity and R (m) is considered the radius of the rotor.

3.4. Computational Domain

The simulation used a CFD method in a 2D framework to analyze the rotor's downstream wake flow. The 2D CFD strategy was nominated for its accuracy in simulating wake flow while minimizing computational costs [36]. A sensitivity analysis focused on three key design parameters to optimize the flow field upstream and downstream of the rotor, thereby reducing the side walls' impact on turbine performance. The critical parameters included " d_i" the distance from the rotor center to the inlet (2D to 15D); " d_o" the distance to the outlet (5D to 40D); and the blockage ratio denoted as D/W, where "W" is the width of the computational domain. The sensitivity analysis results depicted in Figure 3 indicate that alterations to the stator's geometric specifications significantly enhance fluid flow development and mitigate wall influences on turbine performance.

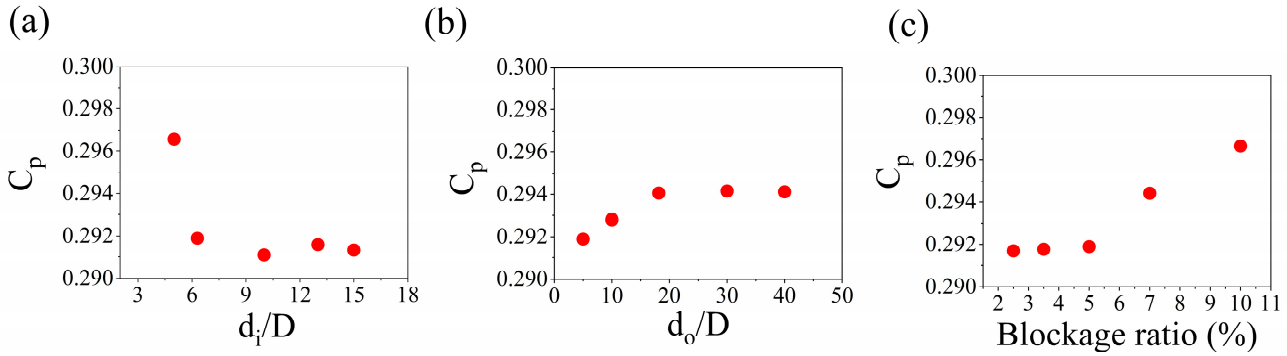


Figure 3. Domain sensitivity analysis. (**a**) Inlet distance effect. (**b**) Outlet distance effect. (**c**) Side wall effect [37].

Figure 3a shows that the estimated C_p for the inlet spans of $2D$ and $5D$ is overstated. The difference in C_p between inlet distances $d_i = 7D$ and $15D$ is minimal (under 1%), so an inlet distance of $7D$ is recommended to reduce overestimation. Figure 3b indicates that as the outlet distance (d_o) increases from 5D to 40D, C_p variability decreases, with only a 0.2% difference noted. Therefore, $d_o = 20D$ is suggested as optimal. In Figure 3c, a blockage ratio of 10% leads to overestimating the C_p due to flow acceleration or deflection. To ensure accurate results, it is recommended to use a domain width $20D$, corresponding to a blockage ratio of 5%. Rezaeiha et al. [38] examined the adverse effects of wall backflow on rotor aerodynamics, highlighting the critical role of the blockage ratio. It is recommended that the blockage ratio remain below 5% to minimize these impacts. The values established for the distances of the inlet, outlet, and lateral sides from the center of the rotor align with findings from numerous prior studies. A schematic and the dimensions of the domain are presented in Figure 1.

3.5. Boundary Conditions

The boundary condition for this simulation is based on the experimental data from Castelli et al. [32], with a constant wind velocity of 9 m/s for the inlet. According to the input data presented by Castelli et al. [32], the Darrieus rotor exhibits an angular velocity that ranges from 24.92 to 57.34 rad/s. In contrast, the angular velocities of the Savonius rotor, as reported in the research conducted by Wenehenubun et al. [33], fall within the range of 5.35 to 27.27 rad/s. The transmission system limits the inner rotor's angular velocity to maintain an acceptable TSR in the low range. To accurately simulate the wind stream outflow, a static gauge pressure of 0 is applied at the outlet to maintain a stationary domain outlet normal to the atmosphere. During the simulation and validation, the boundary condition values such as the inlet wind velocity and outlet pressure conditions will remain constant. Additionally, the angular velocities of both the Darrieus and Savonius rotors will be precisely aligned with these specified parameters throughout the simulation and validation phases. The far field's influence is negligible, so symmetry boundary conditions are applied. A non-slip condition for the turbine walls is essential, and connecting the rotor and stationary domains improves simulation accuracy. The mesh motion technique should also reflect the system's rotation. To elucidate the rotation dynamics of the Darrieus rotor, it is imperative to establish an interface between the rotor and the stationary domain, as well as an additional interface between the Darrieus and Savonius rotors. This approach will facilitate the application of the sliding mesh technique, enabling an accurate simulation of the distinct rotational behavior of the inner rotor, which can operate at varying angular velocities. Implementing a sliding mesh between the inner and outer rotors effectively simulates the functionality of transmission and gearbox systems. The reference experimental simulation was conducted in a low-speed wind tunnel, indicating a turbulence intensity (TI) of 5% at both the inlet and outlet.

3.6. Solver Settings

The investigation employed Ansys Fluent 2021 R2 for the numerical simulations of transient, unsteady flow around the blades. A pressure-based model was chosen to solve momentum and continuity equations appropriate for the incompressible nature of air at low velocities. The SIMPLE (Semi-Implicit Method for Pressure-Linked Equations) scheme was employed for the precise handling of velocity–pressure challenges, efficiently resolving momentum and pressure corrections independently. High-quality fine mesh and small time-step sizes enhanced the algorithm's effectiveness. To ensure accuracy, the second-order upwind method discretized the governing equations for pressure, momentum, turbulence kinetic energy, and specific dissipation rate. Convergence was monitored using the torque

coefficient, deemed convergent when the difference between periods was below 1%, and set with a 10^{-6} threshold, with 30 iterations per time-step. Additionally, the simulation focused on torque fluctuations and output power trends. The results were considered invalid if the torque and power fluctuations did not show a consistent trend. After stabilization, the average power could be used to calculate C_p, and only then was a rotor cycle evaluated for torque on a single blade.

3.7. Mesh Generation Study

Accurate CFD results require careful spatial discretization, mesh refinement, and reliability verification. Proper mesh selection for Savonius and Darrieus rotors is essential for capturing the complex flow behaviors near the airfoil and bucket walls. This simulation used ANSYS-Mesh for problem discretization. A fine-structured mesh of quadrilateral elements was used for the boundary layer mesh inflation to improve accuracy near the blades and buckets, effectively reducing sudden flow variations. Unstructured triangular elements are implemented in the rotating and stationary zones, with a gradual coarsening of the mesh from the airfoil surfaces to the rotor–stator interface. A non-conformal mesh for the sliding interface enhances the mesh density and flux calculation accuracy. The mesh density near the interfaces of the Darrieus rotor and stator, as well as between the Savonius and Darrieus rotors, was coarser than that around the airfoil and bucket walls but finer than the overall domain mesh. This strategic adjustment ensured an enhanced accuracy of the sliding mesh technique during the dual-shaft rotor rotation simulation. Figure 4 displays the detailed mesh for the rotor and stator.

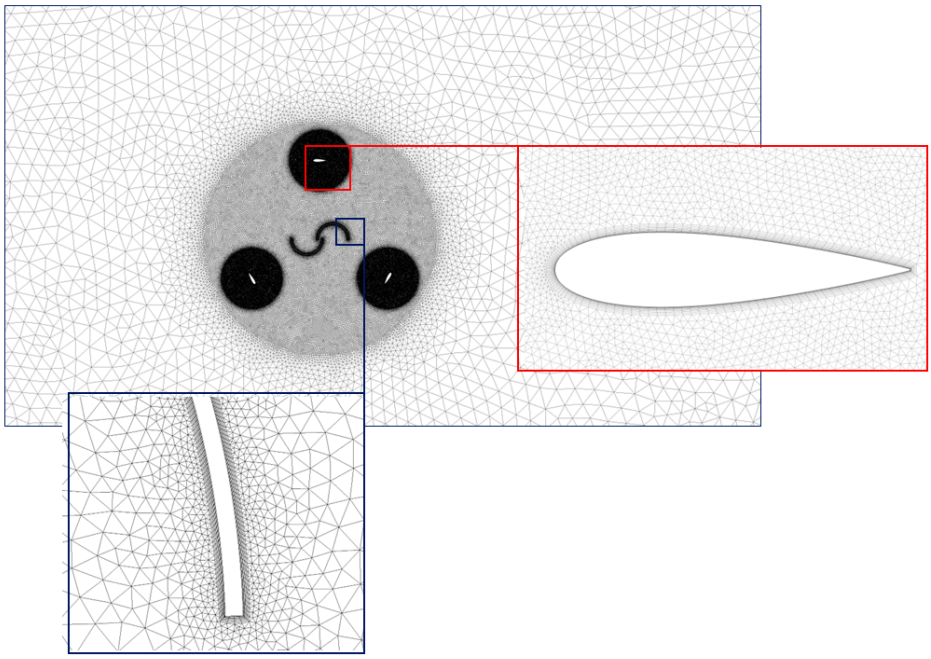


Figure 4. Mesh around the domain, Darrieus blade, and Savonius bucket.

The mesh study examined the single-shaft hybrid Darrieus–Savonius VAWT, assessing four refinements related to mesh size and density around the airfoil and bucket walls. Table 2 outlines the properties of each mesh level, with level 1 being the coarsest and level 4 the finest.

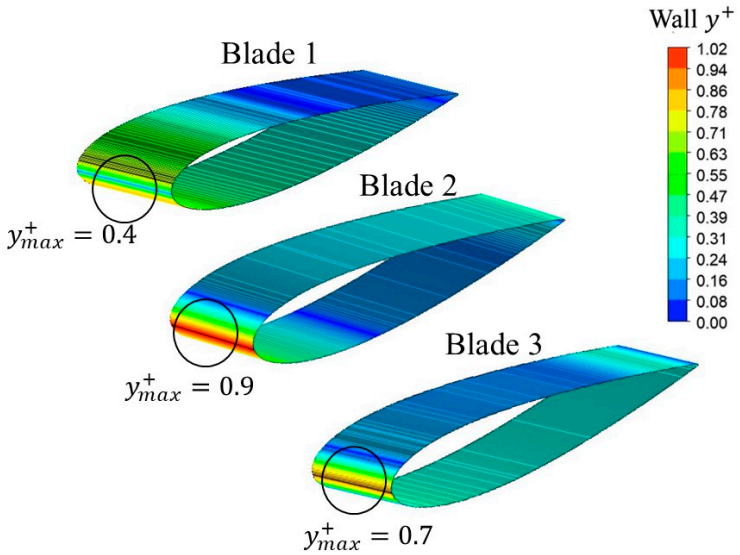
Table 2. Mesh independence summary.

Grid Properties	Mesh Level 1	Mesh Level 2	Mesh Level 3	Mesh Level 4
Number of elements $\times 10^3$	441	564	786	846
Airfoil element size (mm)	0.05	0.03	0.015	0.01
Bucket element size (mm)	0.85	0.64	0.42	0.21
Darrieus number of inflation layers	12	14	16	18
Darrieus first layer thickness (mm)	0.029	0.024	0.019	0.015
Inflation growth rate	1.2	1.15	1.1	1.05
Savonius number of inflation layers	8	10	12	14
Maximum skewness	0.946	0.979	0.969	0.984
Averaged $y+$	1.4	0.9	0.83	0.74
C_p	0.2918	0.2929	0.2939	0.2931

Equation (8) describes y^+, which has a significant impact on the mesh quality. It represents the dimensionless distance perpendicular to the wall and is related to the thickness of the boundary layer [39].

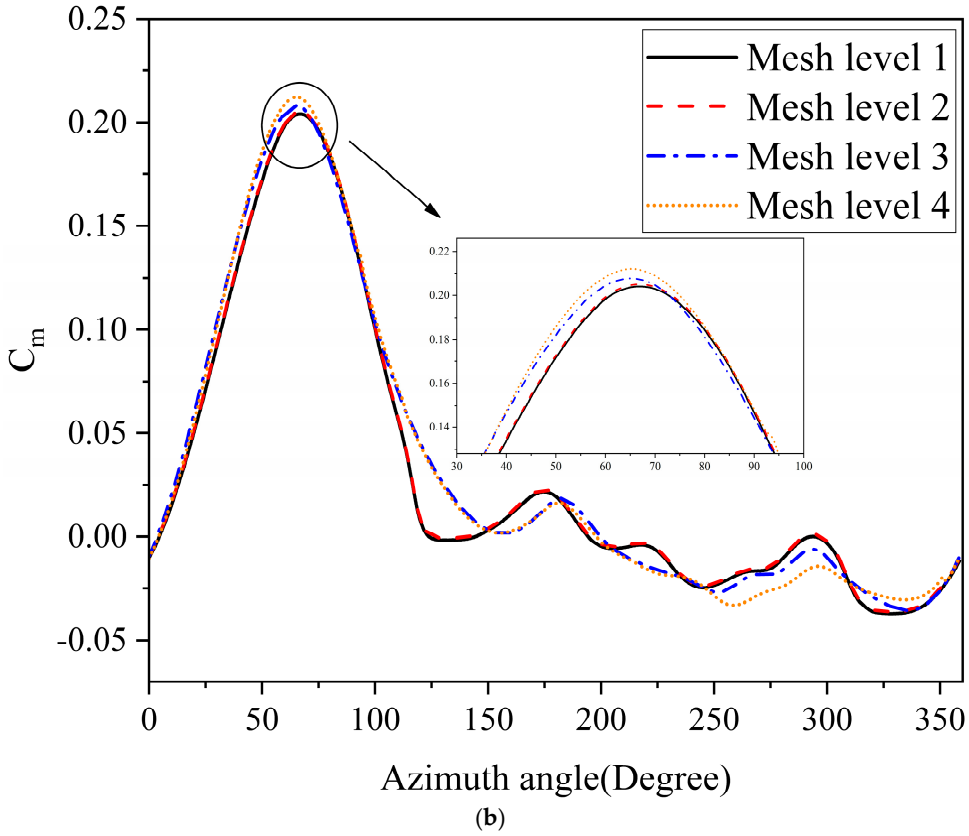
$$y^+ = \frac{\rho_w y u_\tau}{\mu_w} \tag{8}$$

The parameter "y" represents the distance from the mesh center to the blade wall. Here, ρ_w and μ_w are the density and dynamic viscosity of the fluid near the airfoil and bucket walls. Friction velocity, μ_τ, is defined as $\mu_\tau = \sqrt{\frac{\tau_w}{\rho_w}}$, where τ_w is the wall shear stress calculated by $\frac{\mu \partial u}{\partial y}$. For the $k-\omega$ SST turbulence model to function correctly, a y^+ parameter of approximately 1 with a quality mesh is necessary [40]. Figure 5a depicts the optimal y^+ values for the three rotor blades, while Figure 5b presents the static torque diagram for a single blade across different mesh levels.



(**a**)

Figure 5. *Cont.*



(**b**)

Figure 5. (**a**) Wall y^+ contour for the blades. (**b**) Single blade C_m as a function of azimuth angle in a complete rotation at TSR = 2 [37].

Based on Figure 5a, the y^+ values for all blades remain within the acceptable range of 1, showing a decreasing trend from the leading edge to the trailing edge on both the suction and pressure sides. The highest y+ values are observed at the blade tip leading edge, where the wall shear is maximized compared to the airfoil sides and trailing edge. The analysis of the C_p values in Table 2, along with the C_m values for the Darrieus rotor blade during its complete rotation, as shown in Figure 5b, indicates that variations in density and element enumeration have a minimal effect on the single blade C_m. The findings demonstrate that the CFD solution is consistent and independent of mesh count and size, highlighting the significance of the underlying flow physics. Table 2 shows that mesh level 3 provides the highest C_p value, while mesh level 1 yields the lowest, with a less than 1% variation. This reinforces the reliability of the CFD study and its independence from the number of generated elements.

3.8. Time-Step Independence

In CFD tasks, a critical challenge is maintaining data independent from time-step size. This issue is significant in flow simulations for VAWTs, where rapid changes in airflow dynamics near the airfoil surfaces occur, especially at the low-TSR range. These conditions result in increased fluctuations in vorticity fields, highlighting the necessity of preserving results' independence from time-step size [41]. A study determined the optimal time-step size for the current simulation. The findings informed parameter selection for subsequent simulations, enhancing the accuracy and reliability of the results. The study employed the Courant–Friedrichs–Lewy (CFL) criterion, as presented in Equation (9) [42].

$$CFL = \frac{u.\Delta t}{\Delta x} \tag{9}$$

where u denotes the airfoil velocity, Δt is the time-step, and Δx is the average distance between two cell centers on the airfoil. The CFL number helps relate the time increment Δt to the time it takes for a fluid particle with velocity u to pass through a cell of dimension Δx. Equation (10) outlines the relationship between the time-step and azimuth angle at varying angular velocities.

$$\Delta t = \frac{\Delta \theta}{\Omega \cdot \frac{180}{\pi}} \tag{10}$$

where $\Delta\theta$ is denoted as the azimuth angle variations related to rotor rotation and Ω is the angular velocity.

Utilizing a Courant number of approximately 10 in viscous turbomachinery flows is recommended to minimize errors [43]. Table 3 illustrates the CFL numbers for various mesh levels and time-steps at two TSRs of 2 and 3.3. Distinct time-step values arise from assigning a different $\Delta\theta$ for each angular velocity, as indicated in Equation (10). It is expected that these variations will not significantly influence the output data, such as the Cp. Additionally, the CFL remaining within an acceptable range confirms the simulation's independence from time-step selection, ensuring optimal time-step choice.

Table 3. CFL for various spatial and temporal discretization [37].

TSR	ω	$\Delta\theta$ (Degree)	Δt (s)	Δx (mm)			
				2.5 Mesh Level 1	**2.1 Mesh Level 2**	**1.7 Mesh Level 3**	**1.3 Mesh Level 4**
				CFL			
2	35.4	2	0.001	34	39.6	48.4	61.7
		1	0.0005	17	19.8	24.2	30.8
		0.5	0.00025	8.5	9.9	12.1	15.4
		0.1	0.00005	1.7	2	2.4	3
3.3	57.3	2	0.0006	32.6	36.92	45.3	57.61
		1	0.0003	16.3	18.5	22.6	28.8
		0.5	0.00015	8.4	9.2	11.3	14.4
		0.1	0.00003	1.7	1.8	2.2	2.9

According to Table 3, at $\Delta\theta = 0.5°$, the time-steps are $\Delta t = 0.00025$ for TSR = 2 and $\Delta t = 0.00015$ for TSR = 3.3. The CFL number shows a decrease within an acceptable range for both mesh levels 1 and 2. The current findings support the choice of mesh level 2 for CFD modeling due to its finer mesh, which is expected to enhance the simulation's accuracy.

Figure 6 illustrates the variation in C_m and its average values (AVE C_m) for mesh level 2, which were within an acceptable CFL range, focusing on time independence and time-step sensitivity with a flow time of 0.2 s. The graph presents data for four time-step sizes, 0.001 s, 0.0005 s, 0.00025 s, and 0.00005 s, corresponding to $\Delta\theta$ values of 2°, 1°, 0.5°, and 0°, respectively.

Figure 6 reveals that variations in Cm maintain a consistent pattern across all time intervals. Additionally, fluctuations in AVE C_m are minimal, showing only a 1% relative difference as the azimuth angle shifts from 0.1° to 1°.

Following the mesh independence study, it was noted that changes in C_p were minimal beyond mesh Level 2, leading to the decision for discretization. The simulation time-step should be based on $\Delta\theta = 0.5°$, ensuring a CFL number below 10. This time-step is recommended to maintain accuracy in the subsequent simulation process.

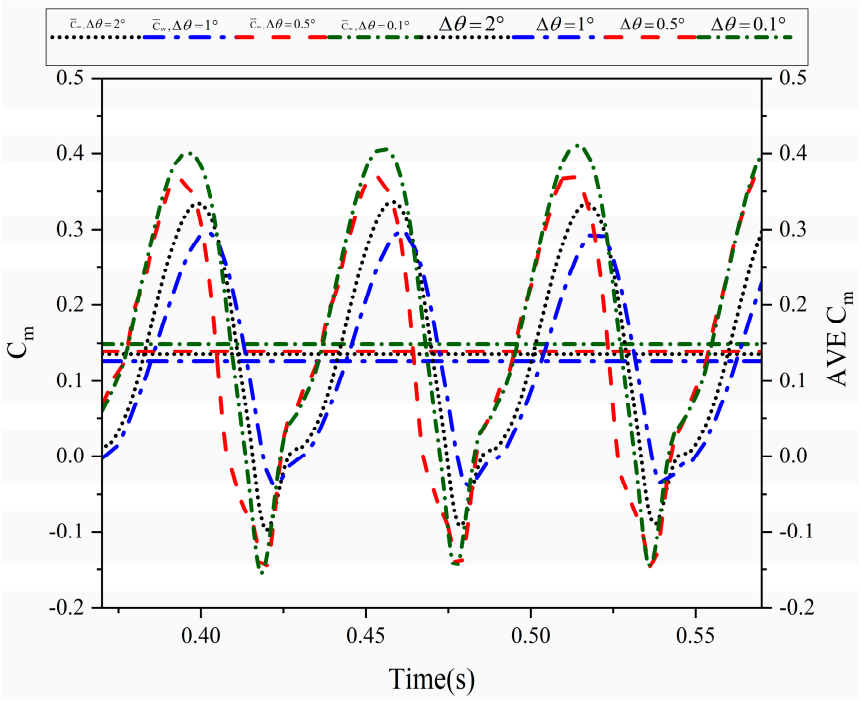


Figure 6. Variation in C_m in relation to time for different time-steps and time-step sensitivity analysis at TSR = 2 [37].

3.9. CFD Model Validation

This study used a double-validation process to ensure the validity of the CFD solution, validating the Darrieus and Savonius rotors separately.

3.9.1. Darrieus Rotor Validation

This study evaluated the control case identified by Castelli et al. [32], comparing their numerical data with numerical and experimental data. Additionally, earlier CFD cases were examined to assess result accuracy and validate the trends shown in the graphs. It is important to note that the experimental study did not consider the blocking effect, resulting in its exclusion from the CFD simulations. The inlet boundary condition was set at 9 m/s, corresponding to the wind tunnel velocity, and the validation process included eight distinct TSRs from 1.4 to 3.3, as illustrated in Figure 7.

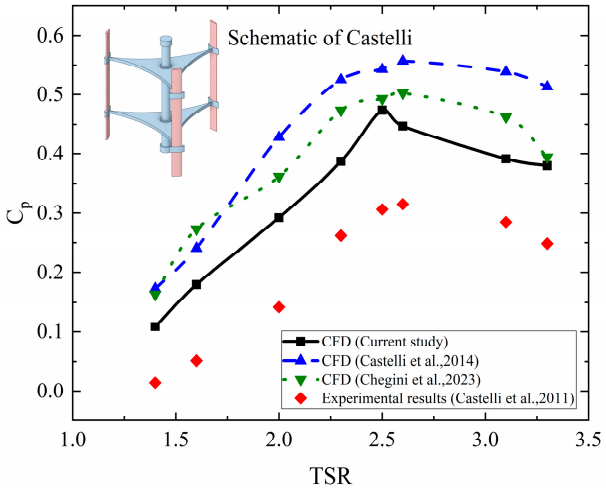


Figure 7. Comparison of Darrieus C_p from the present 2D simulation with experimental and CFD results [32,37,42,44].

To validate our CFD study, we compared our results with empirical data from Castelli et al. [32] and numerical data from Chegini et al. [44] and Castelli et al. [42]. Based on Figure 7, our findings strongly align with empirical and prior CFD data. Notably, our recent CFD results correlate more closely with the empirical data than the numerical results from Chegini et al. [44] and Castelli et al. [42]. However, a discrepancy remains between the experimental data and all CFD outcomes, attributed to simplifications in the 2D solution, the URANS model, and the exclusion of mechanical apparatus like arms and shaft losses.

3.9.2. Savonius Rotor Validation

This section validates the Savonius rotor numerical results by comparing them with Wenehenubun's et al. [33] experimental findings. The experimental study did not consider the blocking effect, as the rotor was placed at the outlet section of the wind tunnel instead of the test section. Consequently, this parameter was omitted in the CFD analysis. The turbulence intensity (TI) and turbulence length scale were set at 1% and 1 m, respectively, using a low-velocity wind tunnel with a range of 1 to 10 m/s; therefore, an inlet boundary condition of 9 m/s was considered. Additionally, the validity of the CFD results was assessed in comparison to another CFD solution by Chegini et al. [44], utilizing four distinct TSRs ranging from 0.4 to 0.51. The validation results are presented in Figure 8.

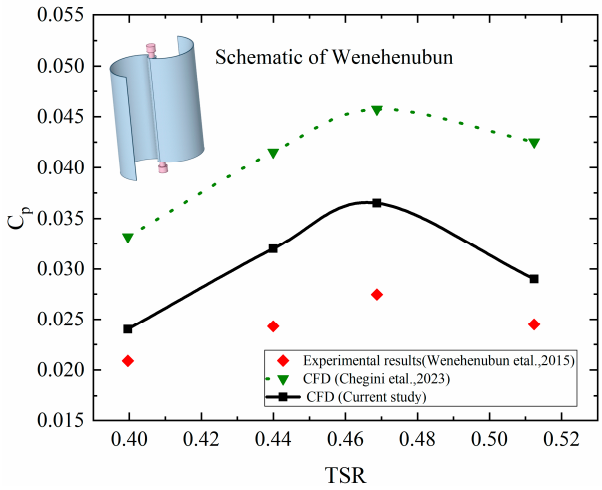


Figure 8. Comparison of Savonius C_p from the present 2D simulation with experimental and CFD results [33,37,44].

The CFD results align closely with experimental findings, peaking at a TSR of 0.469 (ω = 25.4 rad/s), after which the C_p decreases according to the Betz limit. While 2D-modeling and URANS-based methodologies introduced some discrepancies compared to the experiments, the current CFD simulations show improved accuracy over previous results by Chegini et al. [44]. Nevertheless, this study follows the same trend. The maximum deviation from the experimental data was 18% at a TSR of 0.4. The enhanced measurement precision of distances between the inlet, outlet, and side walls significantly reduced the error margin in the current CFD results. The discrepancies observed between the current CFD results and the experimental data, such as those related to the validation of the Darrieus rotor, can be attributed to the limitations of 2D and URANS simulations. Additionally, these discrepancies arise from the failure to account for losses incurred by mechanical components, including arms and shafts.

The CFD solution is considered valid because it meets the established standards from the literature review, mesh generation verification, and time-step analyses. It also demonstrates reliability and aligns with trends observed in previous CFD simulations

and experimental data. It should be noted that in a study of the hybrid rotor, Ghafoorian et al. [37] performed three verification steps, including mesh, time, and validation studies. They were reevaluated and presented again to ensure the robustness of current results. As the 2D simulation was carried out in the mid-plane, the 3D tip effects on the Darrieus rotor blades and Savonius buckets can be considered negligible. Thus, the simulation's accuracy is acceptable for the flow field in this mid-plane assumption.

4. Results and Discussion

This section provides a detailed and systematic examination of a hybrid Darrieus–Savonius VAWT featuring two configurations: a single shaft and a dual shaft. In the dual-shaft configuration, the rotor is managed using a gearless transmission system to prevent the inner rotor's angular velocity from exceeding a predetermined threshold. Accordingly, in the dual-shaft hybrid configuration, the angular velocity of the Savonius rotor is restricted to a range between 5.34 and 27.27 rad/s. In contrast, the Darrieus rotor operates within an angular velocity range of 24.92 to 57.34 rad/s. The dual shaft configuration can facilitate rotation in co-rotating and counter-rotating modes. The performance characteristics are illustrated in Figure 9.

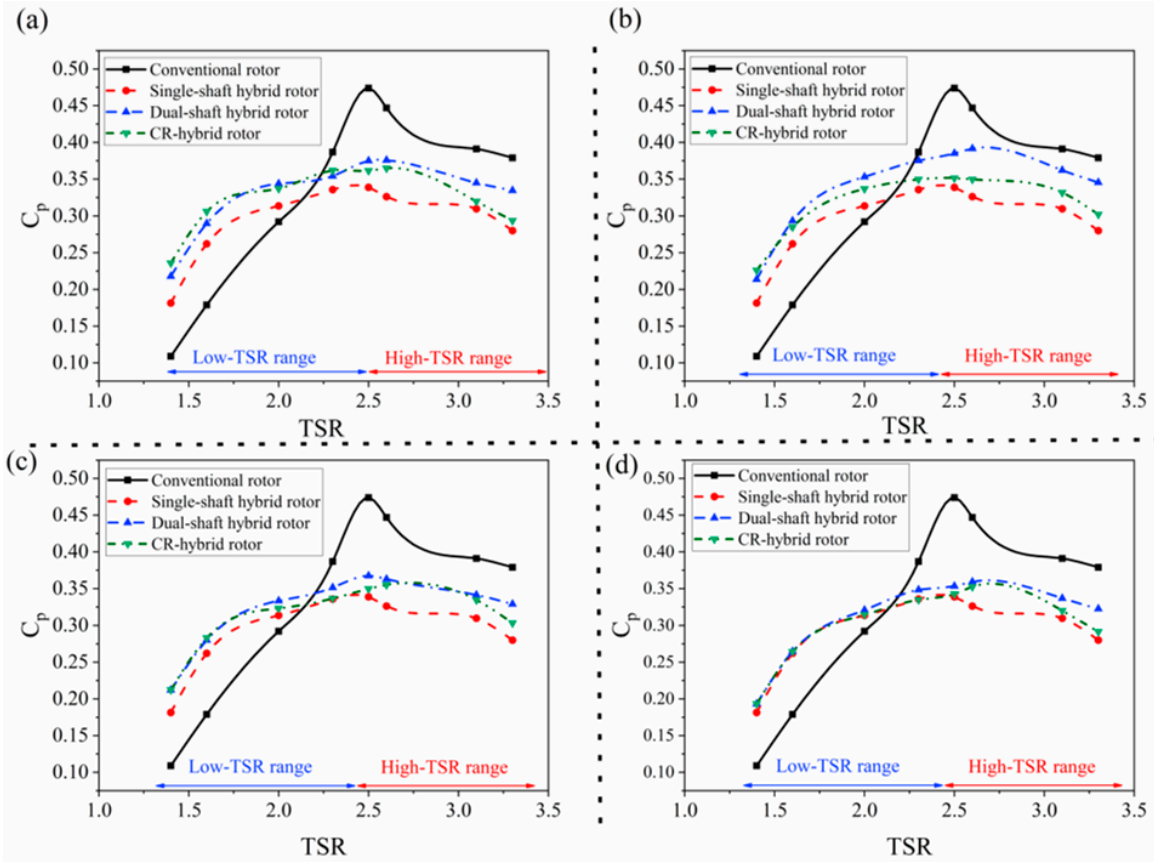


Figure 9. Performance map for different Savonius rotor angular velocities: (**a**) 27.27 rad/s (**b**) 19.79 rad/s (**c**) 12.3 rad/s (**d**) 5.35 rad/s.

According to Figure 9, the hybrid configuration in each configuration markedly enhances the rotor's C_p across a significant portion of the low-TSR range, suggesting an improvement in self-starting capability compared to conventional rotors. Conversely, it was identified that the hybrid configuration exhibits a potential vulnerability in the high-TSR range, leading to a significant decline in the efficiency of the hybrid rotors. This situation resulted in the design of dual-shaft systems. It is well-established that the dual-shaft configuration, whether co-rotating or counter-rotating, demonstrates an enhancement in C_p of

approximately 35% at TSR = 1.4, compared to the single-shaft hybrid rotor. By utilizing a dual-shaft configuration, the significant decline in efficiency observed in the single-shaft hybrid rotor within the high-TSR range was rectified, achieving an enhancement of up to 25% at a TSR = 2.6. Consequently, it can be concluded that the separation of the shafts of the two rotors, facilitated by the implementation of a transmission control mechanism, led to an improvement in the performance of the hybrid Darrieus–Savonius VAWT. Upon examining the particulars, it was supposed that although the counter-rotating hybrid configuration demonstrated superiority over the single-shaft configuration, it does not enhance C_p compared to the co-rotating hybrid configuration. In the low-TSR range, the performance metrics are nearly identical, and only a marginal improvement of approximately 10% at TSR = 1.4 was observed when the Savonius rotor operated at an angular velocity of 27.27 rad/s. Conversely, in the high-TSR range, the counter-rotating configuration exhibits relatively inferior performance compared to the co-rotating configuration, particularly when the Savonius rotor maintains an angular velocity of 19.79 rad/s. The utilization of the transmission system yielded a significantly more favorable impact than the single-shaft hybrid configuration when the angular velocity of the internal rotor was measured at 19.79 rad/s (refer to Figure 9b). This advantageous effect tends to diminish at lower rotational velocities of the internal rotor. When the inner rotor's angular velocity is set at 5.35 rad/s, the dual-shaft configuration has a favorable impact on performance compared to the single-shaft configuration. However, this advantage diminishes compared to configurations operating at higher angular velocities (refer to Figure 9d). Furthermore, there is no significant distinction between the co-rotating and counter-rotating configurations, as both configurations exhibit functionally identical performance characteristics in practice. Consequently, utilizing the transmission system and regulating the Savonius rotor's angular velocity is significant at elevated angular velocities (refer to Figure 9a,b). This observation aligns with the anticipated performance characteristics of VAWTs, as Savonius rotors exhibit optimal efficiency primarily at low angular velocities. The implemented control mechanism effectively mitigates any adverse effects on performance by ensuring that the Savonius rotor's angular velocity does not surpass specified thresholds. Generally, whether operating in a co-rotating or counter-rotating manner, the dual-shaft configuration significantly enhances aerodynamic performance and efficiency compared to a single-shaft rotor across both high- and low-TSR ranges, as the transmission control system efficiently regulates the angular velocity of the Savonius rotor, thereby preventing it from reaching excessive values.

A more comprehensive analysis of the average C_p for various configurations is illustrated in Figure 10.

Figure 10 presents the average C_p values within the operational range of VAWTs across various configurations, facilitating an evaluation of each design's overall efficiency. The single-shaft hybrid rotor demonstrates lower overall efficiency than alternative configurations. This reduction in average efficiency has been associated with the remarkable decline in C_p values for this configuration at the high-TSR range. The analysis demonstrates that while other dual shaft co-rotating and counter-rotating VAWTs have enhanced the performance margin in comparison to the single-shaft rotor by a range of 20% to 6%, only the dual-shaft configuration with a Savonius rotor angular velocity of 19.79 rad/s exhibits a higher AVE C_p than the conventional rotor. Although this dual-shaft configuration experienced a reduction in C_p within the high-TSR range compared to the conventional case, the C_p values in the low-TSR range, as illustrated in the performance map, have shown considerable improvement. This significant enhancement within the low-TSR range is the primary factor contributing to the superior AVE C_p of this configuration, thereby bolstering its self-starting capabilities. Other configurations exhibit lower AVE C_p than the conventional rotor, which is primarily due to a decline in C_p within the high-TSR range.

Furthermore, counter-rotating configurations demonstrate inferior overall performance, with lower AVE C_p values than co-rotating configurations at equivalent Savonius rotor angular velocities. The performance map analysis further confirms that counter-rotating rotors have a comparative disadvantage compared to their co-rotating counterparts.

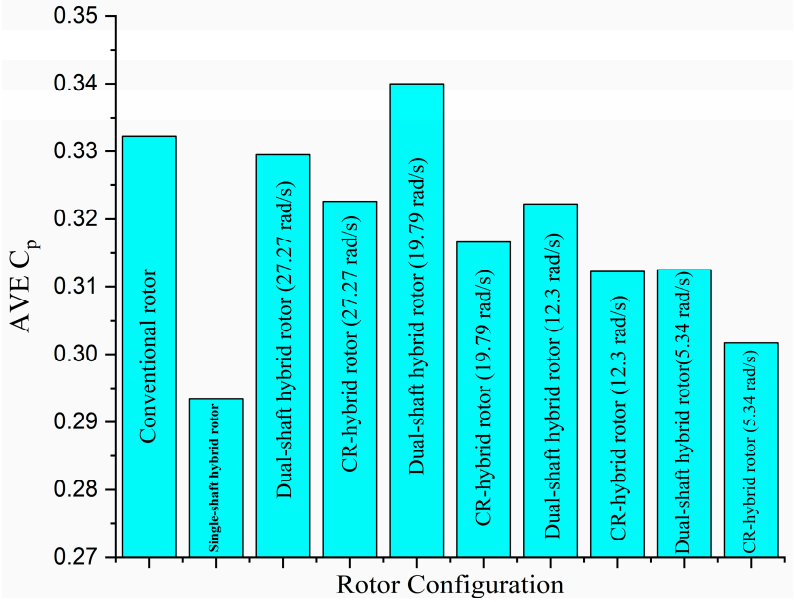


Figure 10. Average C_p for various configurations.

To enhance the understanding of the improvements in self-starting capabilities within a hybrid configuration, analyzing the variable C_m in relation to the azimuth angle is essential. The variation in the azimuth angle during the rotor's transition between distinct regions, such as from the windward section to the upwind area, is significant, as the azimuth angle changes influence both the tangential and normal forces affecting rotor torque during the operation. This relationship is illustrated in Figure 11.

According to Figure 11, the implementation of hybrid configurations resulted in an enhancement of the C_m in comparison to the conventional Darrieus rotor design. This improvement is particularly evident as the Darrieus rotor blade transitions from the azimuth angle of 0°, moving from the windward region to the upwind region. In the conventional configuration, C_m exhibits a negative value at the initiation phase, indicating that the conventional Darrieus VAWT requires initial torque to commence operation. In contrast, both single- and dual-shaft hybrid configurations demonstrate a C_m greater than zero at the azimuth angle of 0°. The advantages of the hybrid configuration are significantly evident across all windward and upwind regions within the azimuth angles ranging from 0° to 135°. In fact, the integration of the conventional Darrieus rotor with the Savonius rotor, which operates as a drag-based impulse turbine and does not necessitate initial torque for initiation rotation, enhances the system's self-starting capability in both dual-shaft and single-shaft configurations. This combination provides the required initial torque at an azimuth angle of 0°. Therefore, the C_m exceeds zero at the rotor's starting point within the windward region. The enhancement of overall C_m in hybrid rotors, regardless of their configuration, during a complete rotation, compared to the conventional Darrieus rotor, was the primary factor contributing to the C_p improvement in the low-TSR range. Furthermore, the dual-shaft configurations, which incorporate effective Savonius rotor angular velocity control, demonstrated a greater improvement in the C_m for the hybrid VAWT compared to the single-shaft configuration. However, similar to the performance map, which indicated

that the distinction between co-rotating and counter-rotating configurations is negligible, the variations in C_m for these two designs exhibit only marginal differences.

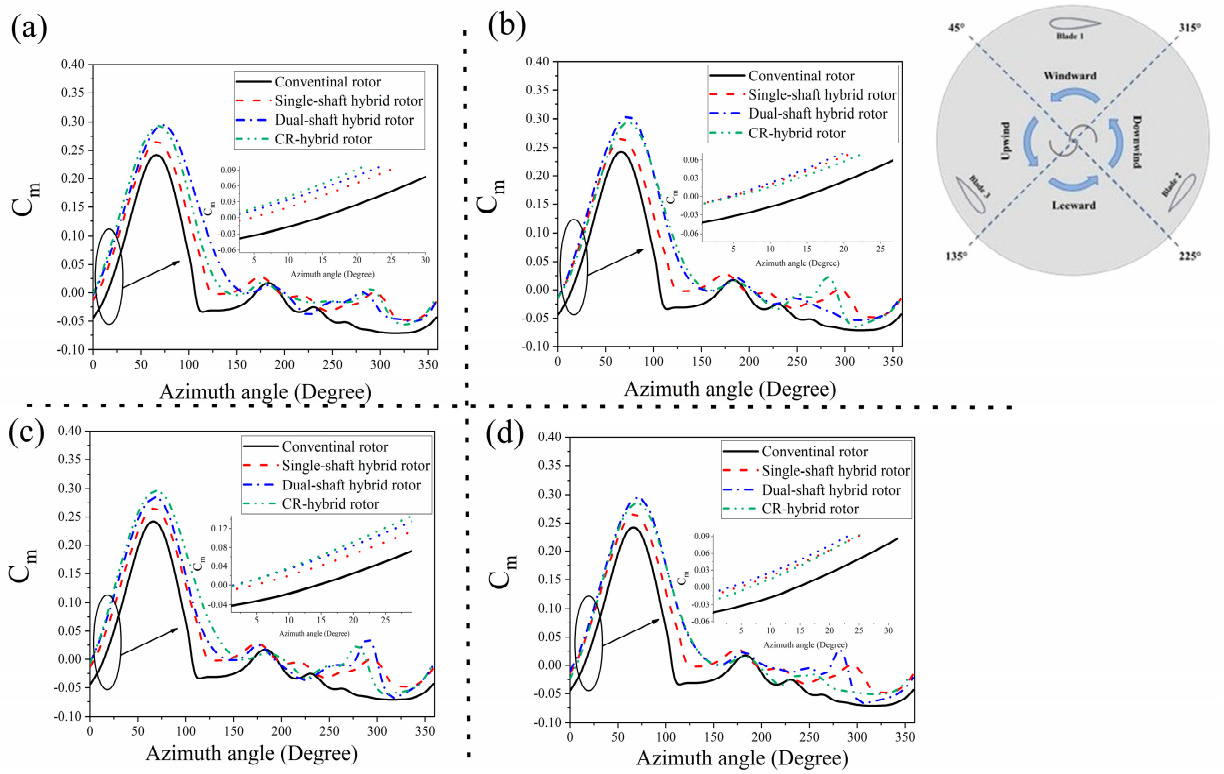


Figure 11. C_m as a function of azimuth angle for one blade for different Savonius rotor angular velocities: (**a**) 27.27 rad/s (**b**) 19.79 rad/s (**c**) 12.3 rad/s (**d**) 5.35 rad/s.

To enhance the understanding of the flow physics involved and the rationale for optimizing the aerodynamic performance of the hybrid rotor, as well as to study the self-starting capability improvements within the dual-shaft configuration when the inner rotor angular velocity is 19.79 rad/s, the pressure field across a single blade is illustrated in Figure 12.

According to Figure 12, when the blade is positioned windward at an azimuth angle of 0°, the positive pressure gradient at its leading edge remains consistent across all configurations. However, as the blade rotates toward the upwind region at azimuth angles of 45° and 90°, the positive pressure gradient on the suction side of the hybrid configurations increases significantly, ranging from 100 to 300 Pa, compared to the conventional rotor. This enhancement contributes to improved torque and self-starting capabilities. At an azimuth angle of 90°, it is evident that a positive pressure gradient develops on the pressure side blade within the conventional configuration. This phenomenon is referred to as an unfavorable pressure gradient, as it inhibits rotor rotation. In contrast, unfavorable pressure gradients in hybrid configurations are restricted primarily to the region near the trailing edge. Furthermore, the magnitude of the positive pressure gradient on the pressure side of dual-shaft rotors, whether co-rotating or counter-rotating, remains lower than that observed in single-shaft configurations, which indicates that the dual-shaft design exhibits superior performance compared to the single-shaft design as a less unfavorable pressure gradient exists at the opposite of the rotor rotation direction, which can disrupt rotor torque. By orienting the rotor towards the leeward region at an azimuth angle of 135°, there is a significant improvement in the positive pressure gradient on the suction side of the hybrid configurations, whether employed in single- or dual-shaft designs, compared to conventional rotor configurations. This enhancement leads to increased torque and

improved self-starting capabilities. Moreover, the unfavorable pressure gradient around the pressure side is alleviated, resulting in a pressure concentration of 300 Pa, which is primarily situated near the trailing edge instead of being fully developed on the suction side. The development and attachment of the unfavorable pressure gradient at the pressure side of a conventional rotor blade led to disturbances in the torque dynamics. This modification greatly aids in facilitating the hybrid rotor's rotation. When the blade is positioned downwind at the azimuth angles of 225° and 315°, the pressure field surrounding the suction and pressure sides are semi-identical, as the C_m values in this region show minimal variation. However, at an azimuth angle of 225°, a pressure gradient of 100 Pa was recorded on the suction side of the dual-shaft rotor blade. This observation indicates a potential enhancement in the aerodynamic performance of this specific configuration. Therefore, implementing the hybrid configuration has enhanced rotor torque and efficiency by establishing a positive pressure gradient on the suction side while mitigating it on the pressure side. Figure 13 illustrates the vorticity field, which can be used to analyze the impact of the Savonius rotor on the performance of the Darrieus rotor.

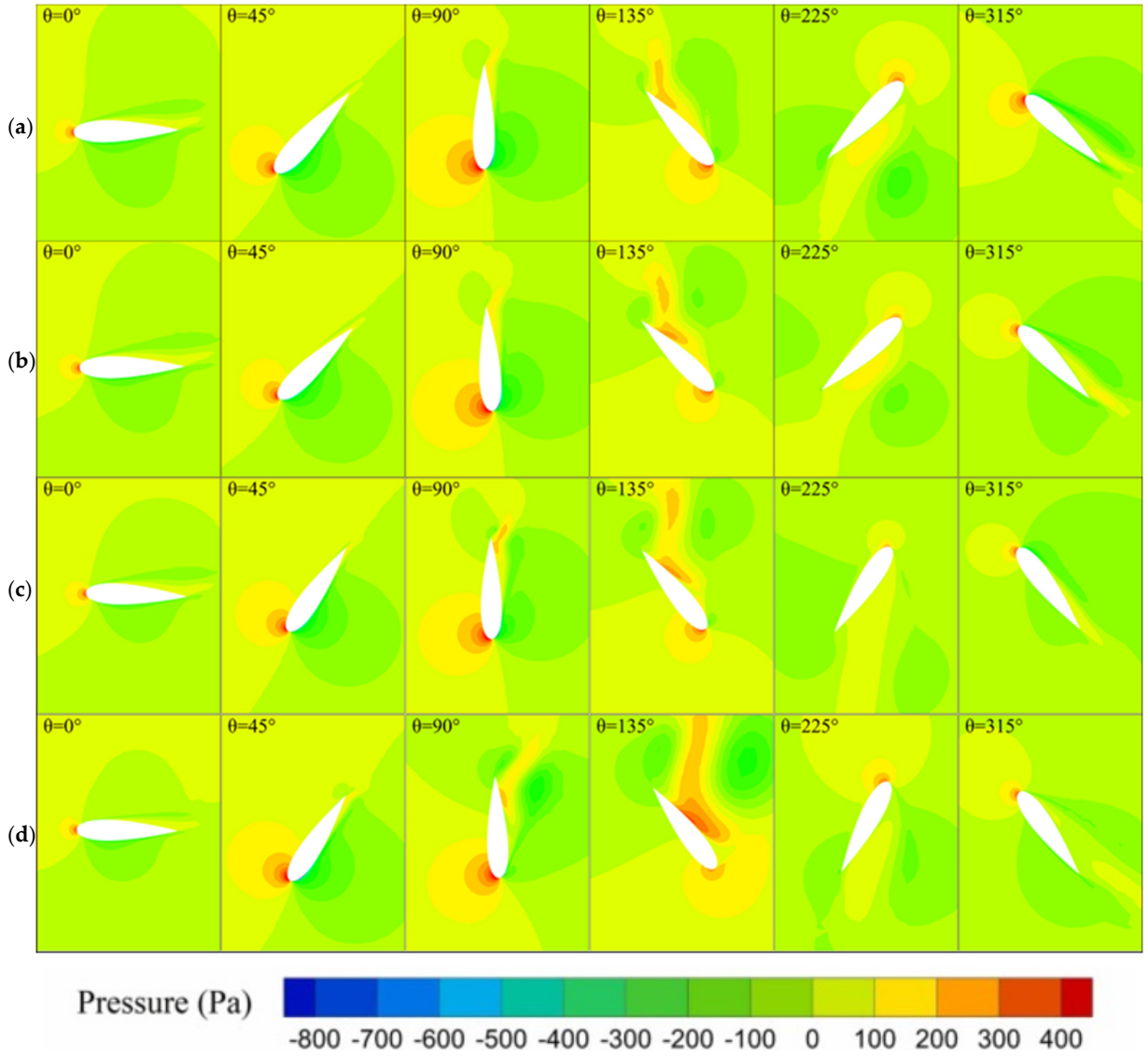


Figure 12. Pressure field around single blade: (**a**) CR hybrid, (**b**) dual-shaft hybrid, (**c**) single-shaft hybrid, (**d**) conventional rotors.

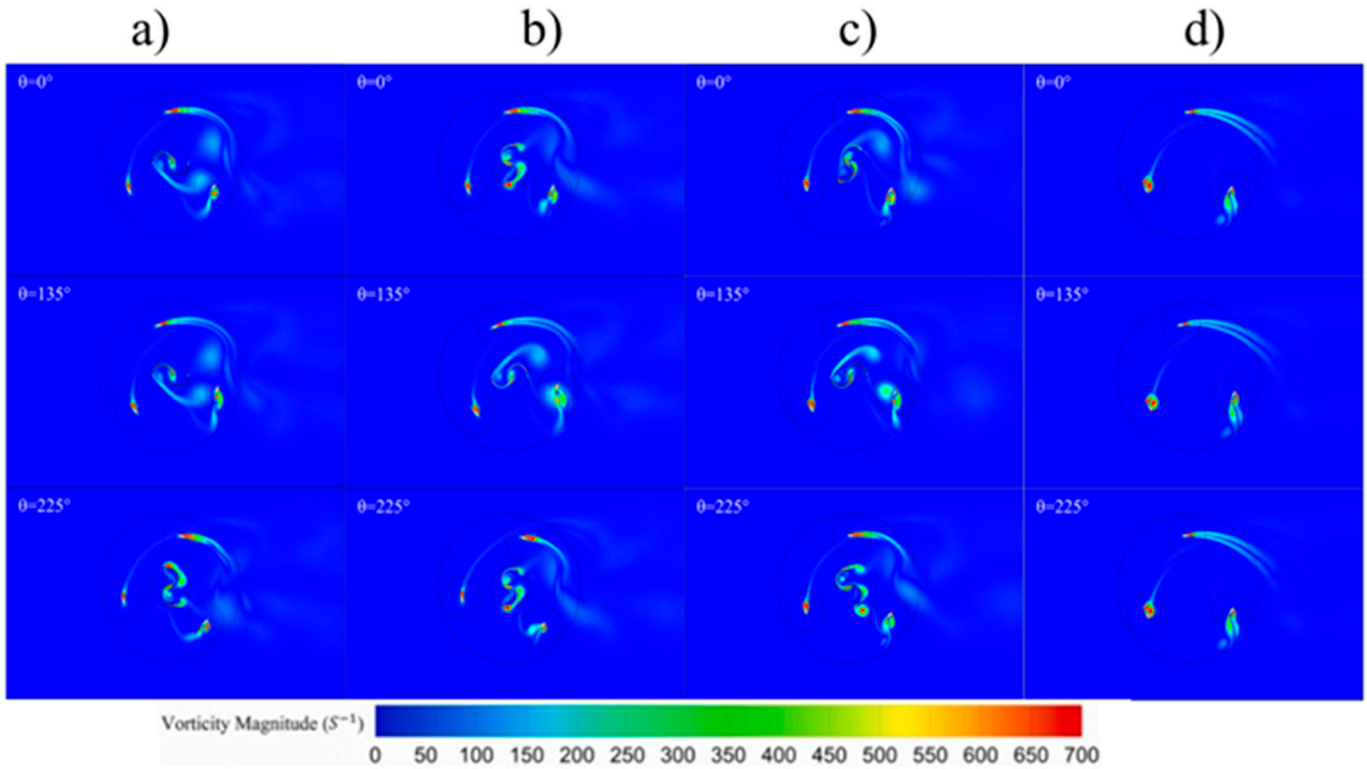


Figure 13. Vorticity magnitude field around single blade: (**a**) CR hybrid, (**b**) dual-shaft hybrid, (**c**) single-shaft hybrid, (**d**) conventional rotors.

Based on Figure 13, the vortices generated around the buckets of the Savonius rotor tend to extend towards the Darrieus rotor, affecting the overall performance. A comparative analysis of the single- and dual-shaft configurations, as depicted in Figure 13b,c, clearly indicates that at all azimuth angles, the single-shaft rotor, represented by the Savonius rotor, operates at an angular velocity equivalent to that of the Darrieus rotor; the intensity of vorticity surrounding the buckets is particularly pronounced, especially at azimuth angles of 0° and 135°. At these specific angles, the distribution of vorticity is notably concentrated, originating from the convex side of the advancing bucket and extending towards the Darrieus rotor. However, in the dual-shaft configuration, where the angular velocity of the inner Savonius rotor is regulated at 19.79 rad/s, which is lower than that of the outer Darrieus rotor, the intensity of the vortices generated around the convex surfaces of both the advancing and returning buckets is diminished. Although these vortices are still extended toward the blades of the Darrieus rotor, their reduced intensity results in a less pronounced negative impact. The reduction in the intensity of vorticities directed toward the Darrieus rotor from the Savonius rotor buckets is clearly observed at the azimuth angles of 135° and 225°. The dual-shaft configuration demonstrates enhanced performance by regulating the angular velocity of the inner rotor, thereby not only reducing unfavorable vortices but also controlling its torque to remain lower than that of the outer rotor. Consequently, the dual-shaft rotor outperforms the single-shaft rotor, which is particularly evident in the higher Cm values observed in the Darrieus rotor blade. This is especially significant at the initial azimuth angles, where the Darrieus rotor requires initial torque (refer to Figure 11). In the configuration of the counter-rotating hybrid rotor, it is evident that the vortices originating from the convex side of the returning bucket directed their flow toward the Darrieus rotor. These vortices exhibited greater intensity at an azimuth angle of 0° compared to the co-rotating configuration, and they developed directly toward the trailing edge of the Darrieus rotor blade. This phenomenon accounts for the reduced effectiveness observed in

the counter-rotating configuration. Utilizing the transmission system, in conjunction with regulating the inner rotor's angular velocity, mitigates the potential for excessive increases in this angular velocity. This regulatory mechanism ensures that the angular velocity of the inner rotor does not reach that of the Darrieus rotor, thereby effectively inhibiting the distribution of vorticity around the buckets and their adverse impact on Darrieus rotor.

5. Conclusions

This research employs CFD with the URANS method and $k-\omega\ SST$ equations to analyze the performance of single- and dual-shaft hybrid Darrieus–Savonius VAWTs. The dual-shaft design features a gearless drivetrain transmission that regulates the inner Savonius rotor's angular velocity to protect the Darrieus rotor's performance from the Savonius buckets' vortices at high angular velocities. This study also examines co-rotating and counter-rotating configurations. Following a comprehensive validation process, the study results are concluded as follows:

- Hybrid turbines, whether single- or dual-shaft, can enhance the rotor's self-starting capability. According to the analysis of power and torque coefficients, the Savonius rotor yields the necessary initial torque for rotation.
- Although the hybrid rotor has improved self-starting capability and increased efficiency in the low-TSR range compared to the conventional Darrieus rotor, its C_p decreased in the high-TSR range.
- The primary justification for enhancing the performance of hybrid rotors within the low-TSR range is rooted in the characteristics of the Savonius VAWT. Unlike the Darrieus VAWT, which operates based on lift force, the Savonius design is a drag-based impulse turbine. This fundamental distinction enables the Savonius rotor to self-start without requiring an initial torque. Consequently, the Savonius rotor effectively generates the initial torque necessary to initiate operation, thereby improving the self-starting capability of hybrid rotors.
- The primary factor contributing to the hybrid rotor's decrease in efficiency within the high-TSR range is the adverse impact of the vorticities generated around the buckets of the Savonius rotor, which are oriented toward the Darrieus rotor. This issue has been partially addressed by implementing a dual-shaft system and regulating the angular velocity of the Savonius rotor, which is inherently designed to operate at lower angular velocities.
- The drivetrain transmission system significantly enhances the efficiency of the dual-shaft rotor compared to the single-shaft configuration, achieving optimal performance when the inner rotor's angular velocity is set to 19.79 rad/s.
- The dual-shaft configuration with a regulated inner rotor angular velocity of 19.79 rad/s enhanced the rotor efficiency by 35% in the low-TSR range compared to the traditional single-shaft rotor. Additionally, it mitigated the inefficiencies associated with the single-shaft rotor in the high-TSR range by 25%.
- While the counter-rotating configuration exhibits superior performance compared to the single-shaft configuration, its performance is either weaker or comparable to that of the co-rotating configuration.
- The performance differences among the single-shaft, co-rotating, and counter-rotating configurations of the Savonius rotor become less pronounced at lower rotational velocities. This observation underscores that the drivetrain transmission system's beneficial impact is more evident at higher inner rotor revolutions.

As a result, the hybridization of the Darrieus rotor, in conjunction with the Savonius rotor, has demonstrated the potential to enhance self-starting capabilities. Furthermore, implementing a control mechanism facilitated by integrating a transmission system within

the dual-shaft rotor amplifies this improvement and effectively addresses the challenge of efficiency losses in the high-TSR range. This indicates that the hybrid design presents a viable solution for various applications in renewable energy systems, including VAWTs for on-highway use and residential rooftop installations.

6. Future Study

In the context of this CFD study, certain limitations in simulation were identified. The design selected for this CFD analysis features a Darrieus VAWT with a diameter of 1 m and a height of 1.5 m. While these dimensions are appropriate for the practical applications of the turbine, it is advisable to conduct an investigation into the aspect ratio of the Darrieus rotor, as well as to analyze the diameter ratio between the Darrieus rotor and the Savonius rotor to ensure the installation feasibility of the hybrid rotor and optimum performance. This additional research will facilitate the identification of optimal dimensions for both rotor types and help to establish the appropriate ratio between the inner and outer rotor diameters. A comprehensive 3D analysis is advisable to achieve more precise CFD results. This approach will also facilitate a clearer understanding of the arrangement of the Savonius rotor in relation to the Darrieus rotor. Consequently, this will aid in determining the optimal selection between a dual or single hybrid rotor configuration in practical applications. Furthermore, the shaft design should be approached as an inner and outer rotor system or a two-stage turbine. It is essential to ascertain whether the Savonius rotor should be positioned above or below the Darrieus rotor in the proposed configuration.

Although hybrid models, including both dual- and single-shaft designs, have demonstrated improvements in the self-starting capabilities of the rotor, further investigation into the dynamics and control mechanisms is advisable. Such a study should aim to evaluate, optimize, and select the most effective transmission system and control strategy. Furthermore, it is advisable to conduct an analysis focusing on different blade types to investigate the influence of blade roughness on efficiency and self-starting capabilities, which can only be effectively achieved through a Large Eddy Simulation (LES) approach.

Author Contributions: Conceptualization, M.M.; Methodology, F.G. and M.M.; Software, F.G. and S.H.R.; Validation, F.G.; Formal analysis, F.G. and S.H.R.; Investigation, F.G.; Data curation, F.G.; Writing—original draft, F.G.; Writing—review & editing, F.G. and S.H.R.; Visualization, S.H.R.; Supervision, M.M.; Project administration, M.M. All authors have read and agreed to the published version of the manuscript.

Funding: This research received no external funding.

Data Availability Statement: The original contributions presented in this study are included in the article. Further inquiries can be directed to the corresponding author.

Conflicts of Interest: The authors declare no conflict of interest.

Nomenclature

Symbols

V_∞	Inlet velocity (m/s)
A	Swept Area (m^2)
T	Torque (N·m)
P	Output power (W)
R	Rotor radius (m)
c	Blade chord length
C_p	Power coefficient
C_m	Torque coefficient

Abbreviations

VAWT	Vertical axis wind turbine
HAWT	Horizontal axis wind turbine
CFD	Computational fluid dynamic
CFL	Courant number
URANS	Unsteady Reynolds-averaged Naiver–Stokes
TSR	Tip speed ratio
CR	Counter rotating

Greek

θ	Azimuth angle (Degree)
ω	Angular velocity (rad/s)
ρ	Density (kg/m^3)

References

1. Mehrpooya, M.; Ghorbani, B.; Khalili, M. A new developed integrated process configuration for production of hydrogen chloride using geothermal and wind energy resources. *Sustain. Energy Technol. Assess.* **2021**, *45*, 101173. [CrossRef]
2. Rosato, A.; Perrotta, A.; Maffei, L. Commercial Small-Scale Horizontal and Vertical Wind Turbines: A Comprehensive Review of Geometry, Materials, Costs and Performance. *Energies* **2024**, *17*, 3125. [CrossRef]
3. Ahmad, M.; Shahzad, A.; Qadri, M.N.M. An overview of aerodynamic performance analysis of vertical axis wind turbines. *Energy Environ.* **2023**, *34*, 2815–2857. [CrossRef]
4. Seifi Davari, H.; Seify Davari, M.; Botez, R.M.; Chowdhury, H. Advancements in vertical axis wind turbine technologies: A comprehensive review. *Arab. J. Sci. Eng.* **2024**, 1–48. [CrossRef]
5. Chitura, A.G.; Mukumba, P.; Lethole, N. Enhancing the Performance of Savonius Wind Turbines: A Review of Advances Using Multiple Parameters. *Energies* **2024**, *17*, 3708. [CrossRef]
6. Fatahian, E.; Mishra, R.; Jackson, F.F.; Fatahian, H. Optimization and analysis of self-starting capabilities of vertical axis wind turbine pairs: A CFD-Taguchi approach. *Ocean Eng.* **2024**, *302*, 117614. [CrossRef]
7. Moradi Ghareghani, M.S.; Abdolahifar, A.; Karimian, S.M.H. Numerical investigation on the helix angle to smoothen aerodynamic torque output of the 3-PB Darrieus vertical axis wind turbine. *J. Wind Eng. Ind. Aerodyn.* **2023**, *234*, 105323. [CrossRef]
8. Reddy, K.U.; Deb, B.; Roy, B. Experimental Study on Influence of Aspect Ratio and Auxiliary Blade Profile on the Performance of H-Type Darrieus Wind Rotor. *Arab. J. Sci. Eng.* **2024**, *49*, 1913–1929. [CrossRef]
9. Shchur, I.; Klymko, V.; Xie, S.; Schmidt, D. Design Features and Numerical Investigation of Counter-Rotating VAWT with Co-Axial Rotors Displaced from Each Other along the Axis of Rotation. *Energies* **2023**, *16*, 4493. [CrossRef]
10. Tahani, M.; Razavi, M.; Mirhosseini, M.; Astaraei, F.R.; Mirmahdian, S. Unsteady aerodynamic performance of Dual-Row H-Darrieus vertical axis wind turbine. *Energy Equip. Syst.* **2020**, *8*, 55–80.
11. Khalid, M.S.U.; Portocarrero Mendoza, P.S.; Wood, D.; Hemmati, A. On the aerodynamics of dual-stage co-axial vertical-axis wind turbines. *Wind Eng.* **2024**, *48*, 408–424. [CrossRef]
12. Kumar, Y.; Roga, S.; Wanmali, N.K. Experimental analysis of hybrid VAWT and the effect of semi-cylindrical attachment to the trailing edge. *Energy Sustain. Dev.* **2023**, *74*, 115–126. [CrossRef]
13. Wakui, T.; Tanzawa, Y.; Hashizume, T.; Nagao, T. Hybrid configuration of Darrieus and Savonius rotors for stand-alone wind turbine-generator systems. *Electr. Eng. Jpn.* **2005**, *150*, 13–22. [CrossRef]
14. Hosseini, A.; Goudarzi, N. Design and CFD study of a hybrid vertical-axis wind turbine by employing a combined Bach-type and H-Darrieus rotor systems. *Energy Convers. Manag.* **2019**, *189*, 49–59. [CrossRef]
15. Roshan, A.; Sagharichi, A.; Maghrebi, M.J. Nondimensional Parameters' Effects on Hybrid Darrieus–Savonius Wind Turbine Performance. *J. Energy Resour. Technol.* **2020**, *142*, 011202. [CrossRef]
16. Asadi, M.; Hassanzadeh, R. Effects of internal rotor parameters on the performance of a two bladed Darrieus-two bladed Savonius hybrid wind turbine. *Energy Convers. Manag.* **2021**, *238*, 114109. [CrossRef]
17. Pan, J.; Ferreira, C.; Van Zuijlen, A. Performance analysis of an idealized Darrieus–Savonius combined vertical axis wind turbine. *Wind Energy* **2024**, *27*, 612–627. [CrossRef]
18. Abdelsalam, A.M.; Kotb, M.A.; Yousef, K.; Sakr, I.M. Performance study on a modified hybrid wind turbine with twisted Savonius blades. *Energy Convers. Manag.* **2021**, *241*, 114317. [CrossRef]
19. Mohan Kumar, P.; Surya, M.R.; Sivalingam, K.; Lim, T.-C.; Ramakrishna, S.; Wei, H. Computational Optimization of Adaptive Hybrid Darrieus Turbine: Part 1. *Fluids* **2019**, *4*, 90. [CrossRef]
20. Zhang, J.; Wang, C.; Liu, W.; Zhu, J.; Yan, Y.; Zhao, H. Optimization of the Energy Capture Performance of the Lift-Drag Hybrid Vertical-Axis Wind Turbine Based on the Taguchi Experimental Method and CFD Simulation. *Sustainability* **2023**, *15*, 8848. [CrossRef]
21. Jacob, J.; Chatterjee, D. Design methodology of hybrid turbine towards better extraction of wind energy. *Renew. Energy* **2019**, *131*, 625–643. [CrossRef]
22. Pouransari, Z.; Behzad, M. Numerical investigation of the aerodynamic performance of a hybrid Darrieus-Savonius wind turbine. *Wind Eng.* **2024**, *48*, 3–14. [CrossRef]
23. Shouman, M.R.; Helal, M.M. Numerical investigation of improvement of counter rotating Savonius turbines performance with curtaining and fin addition on blade. *Alex. Eng. J.* **2023**, *75*, 233–242. [CrossRef]
24. Didane, D.H.; Saipul Anuar, M.A.Z.; Mohideen Batcha, M.F.; Abdullah, K.; Mohd Ali, M.F.; Mohammed, A.N. Simulation Study on the Performance of a Counter-rotating Savonius Vertical Axis Wind Turbine. *CFD Lett.* **2020**, *12*, 4. [CrossRef]

25. Didane, D.H.; Rosly, N.; Zulkafli, M.F.; Shamsudin, S.S. Performance evaluation of a novel vertical axis wind turbine with coaxial contra-rotating concept. *Renew. Energy* **2018**, *115*, 353–361. [CrossRef]
26. Didane, D.H.; Rosly, N.; Zulkafli, M.F.; Shamsudin, S.S. Numerical investigation of a novel contra-rotating vertical axis wind turbine. *Sustain. Energy Technol. Assess.* **2019**, *31*, 43–53. [CrossRef]
27. Poguluri, S.K.; Lee, H.; Bae, Y.H. An investigation on the aerodynamic performance of a co-axial contra-rotating vertical-axis wind turbine. *Energy* **2021**, *219*, 119547. [CrossRef]
28. Kutt, F.; Blecharz, K.; Karkosiński, D. Axial-Flux Permanent-Magnet Dual-Rotor Generator for a Counter-Rotating Wind Turbine. *Energies* **2020**, *13*, 2833. [CrossRef]
29. Shchur, I.; Klymko, V. Comparison of different types of electromechanical systems for creating the counter-rotating VAWT. In Proceedings of the 2017 IEEE First Ukraine Conference on Electrical and Computer Engineering (UKRCON), Kyiv, Ukraine, 29 May–2 June 2017; IEEE: New York, NY, USA, 2017; pp. 373–378.
30. Erturk, E.; Sivrioglu, S.; Bolat, F.C. Analysis Model of a Small Scale Counter-Rotating Dual Rotor Wind Turbine with Double Rotational Generator Armature. *Int. J. Renew. Energy Res.* **2018**, *8*, 1849–1858. [CrossRef]
31. Aladwani, H.A.H.R.; Ariffin, M.K.A.; Mustapha, F. A supervised machine-learning method for optimizing the automatic transmission system of wind turbines. *Eng. Solid Mech.* **2022**, *10*, 35–56. [CrossRef]
32. Raciti Castelli, M.; Englaro, A.; Benini, E. The Darrieus wind turbine: Proposal for a new performance prediction model based on CFD. *Energy* **2011**, *36*, 4919–4934. [CrossRef]
33. Wenehenubun, F.; Saputra, A.; Sutanto, H. An Experimental Study on the Performance of Savonius Wind Turbines Related With The Number Of Blades. *Energy Procedia* **2015**, *68*, 297–304. [CrossRef]
34. Sheidani, A.; Salavatidezfouli, S.; Stabile, G.; Rozza, G. Assessment of URANS and LES methods in predicting wake shed behind a vertical axis wind turbine. *J. Wind Eng. Ind. Aerodyn.* **2023**, *232*, 105285. [CrossRef]
35. Borzuei, D.; Moosavian, S.F.; Farajollahi, M. On the Performance Enhancement of the Three-Blade Savonius Wind Turbine Implementing Opening Valve. *J. Energy Resour. Technol.* **2021**, *143*, 11. [CrossRef]
36. Tescione, G.; Ragni, D.; He, C.; Simão Ferreira, C.J.; Van Bussel, G.J.W. Near wake flow analysis of a vertical axis wind turbine by stereoscopic particle image velocimetry. *Renew. Energy* **2014**, *70*, 47–61. [CrossRef]
37. Ghafoorian, F.; Mirmotahari, S.R.; Eydizadeh, M.; Mehrpooya, M. A systematic investigation on the hybrid Darrieus-Savonius vertical axis wind turbine aerodynamic performance and self-starting capability improvement by installing a curtain. *Next Energy* **2025**, *6*, 100203. [CrossRef]
38. Rezaeiha, A.; Kalkman, I.; Blocken, B. Effect of pitch angle on power performance and aerodynamics of a vertical axis wind turbine. *Appl. Energy* **2017**, *197*, 132–150. [CrossRef]
39. Lositaño, I.C.M.; Danao, L.A.M. Steady wind performance of a 5 kW three-bladed H-rotor Darrieus Vertical Axis Wind Turbine (VAWT) with cambered tubercle leading edge (TLE) blades. *Energy* **2019**, *175*, 278–291. [CrossRef]
40. Marsh, P.; Ranmuthugala, D.; Penesis, I.; Thomas, G. The influence of turbulence model and two and three-dimensional domain selection on the simulated performance characteristics of vertical axis tidal turbines. *Renew. Energy* **2017**, *105*, 106–116. [CrossRef]
41. Balduzzi, F.; Bianchini, A.; Ferrara, G.; Ferrari, L. Dimensionless numbers for the assessment of mesh and timestep requirements in CFD simulations of Darrieus wind turbines. *Energy* **2016**, *97*, 246–261. [CrossRef]
42. Trivellato, F.; Castelli, M.R. On the Courant–Friedrichs–Lewy criterion of rotating grids in 2D vertical-axis wind turbine analysis. *Renew. Energy* **2014**, *62*, 53–62. [CrossRef]
43. Menter, F.R. Review of the shear-stress transport turbulence model experience from an industrial perspective. *Int. J. Comput. Fluid Dyn.* **2009**, *23*, 305–316. [CrossRef]
44. Chegini, S.; Asadbeigi, M.; Ghafoorian, F.; Mehrpooya, M. An investigation into the self-starting of darrieus-savonius hybrid wind turbine and performance enhancement through innovative deflectors: A CFD approach. *Ocean Eng.* **2023**, *287*, 115910. [CrossRef]

Disclaimer/Publisher's Note: The statements, opinions and data contained in all publications are solely those of the individual author(s) and contributor(s) and not of MDPI and/or the editor(s). MDPI and/or the editor(s) disclaim responsibility for any injury to people or property resulting from any ideas, methods, instructions or products referred to in the content.